

1

2

3

4

Storage and Transport of Charge in Redox Conductive Polymers Probed with Electron Spin Resonance Spectroscopy

5

Ilia Romanovich Kulikov

6

7

8

Im Fachbereich Physik der Freien Universität Berlin eingereichte
Dissertation zur Erlangung des Grades eines
Doktors der Naturwissenschaften

9

10

Berlin
August 2023

11

12

13

14

Erster Gutachter: Prof. Dr. Jan Behrends

Zweiter Gutachter: Prof. Dr. Kirill Bolotin

Tag der Disputation:

15 Contents

16	1 Introduction	7
17	2 Electrochemical Energy Storage in Redox Conductive Polymers	9
18	2.1 Redox Conductive Polymers	9
19	2.2 Organic Radical Battery	9
20	2.3 TEMPO-Salen Cathode Material	10
21	3 Operando EPR Spectroscopy of TEMPO-Salen Cathode Films	11
22	3.1 Electron Paramagnetic Resonance	11
23	3.1.1 The Spin Hamiltonian	11
24	3.1.2 Instrumentation	13
25	3.2 EPR Spectroscopy of a Charging Electrochemical Cell	13
26	3.2.1 Fabrication of EPR-compatible Electrochemical Cells	14
27	3.2.2 cwEPR Spectra During a Charge-Discharge Cycle	14
28	3.2.3 Spectral Simulations	15
29	3.2.4 Quantitative Analysis of Potential-Dependent EPR Spectra	15
30	3.2.5 EPR-Detected State Of Charge	15
31	3.2.6 Formation of Singlet Spin States in a Reduced Cathode Film	15
32	3.2.7 Monitoring of Degradation Processes	15
33	3.2.8 Monitoring of Self Discharge	15
34	3.2.9 Electrochemical Cells with Solid Electrolyte	15
35	3.2.10 Low Temperature Measurements	15
36	4 pEPR Spectroscopy of Densely Packed Nitroxide Radicals	17
37	4.1 Coherent Spin Motion under Pulsed Microwave Field	17
38	4.1.1 Bloch Equations	17
39	4.1.2 Spin Relaxation Times	17
40	4.1.3 Spin Packets	17
41	4.2 Instrumentation	17
42	4.2.1 Pulse Sequences and Measurement Techniques	17
43	4.2.2 Broad-Band Excitation and Instantaneous Diffusion	18
44	4.3 Pulsed EPR Spectroscopy of a charged pDiTBuS Cathode film	18
45	4.3.1 Field Swept Echo of a charged pDiTBuS Cathode film	18
46	4.3.2 Estimation of Local Spin Concentrations with Instantaneous Diffusion	18
47	4.3.3 Spin Relaxation in a charged pDiTBuS Cathode Film	18
48	4.4 Padé-Laplace Deconvolution of Polyexponential Decay Signals	18
49	4.4.1 Padé-Laplace Deconvolution of the Echo-Decay and Inversion-Recovery Transients	21
50	4.4.2 Detection of Domains with Poor Conductivity	27
51	4.4.3 Towards Imaging of Spin Concentration in Battery Electrodes	27
52	4.4.4 Unusual Peak Ratios in a Highly Charged Cathode Film	28

53	5 Longitudinally Detected Electron Paramagnetic Resonance in Systems with Short Relaxation Times	29
55	6 Electrically Detected Magnetic Resonance on a Cathode of an Organic Radical Battery	31
56	6.0.1 Spin Blockade and Spin-Dependent Recombination	31
57	6.0.2 Instrumentation	31
58	6.0.3 Device Fabrication	31
59	6.0.4 EDMR signal in a 1N4007 Si Diode	32
60	6.0.5 EDMR signal in an Organic Field Effect Transistor	32
61	6.0.6 EDMR signal in a TEMPO-Salen Electrochemical Cell	32
62	6.0.7 Distribution of Current Density in On-Substrate Meander-Shaped Electrodes	32
63	7 The Deep-Trap Model of a TEMPO-Salen Electrode Film	35
64	8 Conclusions and Outlook	37

$\vec{e}_x, \vec{e}_y, \vec{e}_z, t$	Laboratory frame of reference
$\hat{\vec{S}} = (\hat{S}_x, \hat{S}_y, \hat{S}_z)$	Spin operator
$h = 6.62607015 \times 10^{-34} \text{ J} \times \text{s}$	Planck constant
$g_e = -2.00231930436118(27)$	Electron g factor
$\mu_B = 9.2740100783(28) \times 10^{-24} \text{ J/T}$	Bohr magneton
$\mu_0 = 1.25663706212(19) \times 10^{-6} \text{ N/A}^2$	Permeability of free space
ϵ	Relative permittivity
$\vec{B}_0 = B_0 \vec{e}_z$	Static magnetic field
cwEPR	Continuous wave electron paramagnetic resonance
pEPR	Pulsed electron paramagnetic resonance
EDMR	Electrically detected magnetic resonance
DUT	Device under testing
ORB	Organic radical battery
WE	Working electrode (cathode, “+”)
CE	Counter electrode (anode, “-”)
RE	Reference electrode
SoC	State of charge
ESOC	EPR-detected SoC
CV	Cyclic voltammogram
GCD	Galvanostatic charge-discharge
TEMPO	2,2,6,6-tetramethylpiperidine-1-oxyl
pDiTS	Poly-di-TEMPO-Salen
pDiTBuS	Poly-di-TEMPO-Butyl-Salen
PTMA	Poly-TEMPO-methacrylate
EDFS	Echo-detected field sweep
ID	Instantaneous diffusion
T_1	Spin-lattice relaxation time
T_m	Phase memory time
t_d	Microwave detector dead time

Table 1: List of abbreviations

65 **Chapter 1**

66 **Introduction**

67 Life needs energy to continue its spread. Plants use photosynthesis to separate carbon from oxygen
68 and to grow. Higher life forms as humans consume energy during the day and during the night, being
69 dependent on the available energy source [?]. While fossil fuels are still the major source of energy [?]
70 and while fire is used to convert the Joules that hold together hydrocarbon molecules into a "horse power"
71 of a combustion engine and kilowatt-hours in a power socket, there are cleaner and more efficient ways
72 to harvest energy. Photosynthesis had inspired the creation of solar panels that convert the sunlight into
73 electricity, the atom had been tamed in the core of a nuclear reactor to power cities; we can extract energy
74 from sound [?], wind and waves and from the heat of the planet. Moreover, there are hopes and contin-
75 uous attempts to achieve nuclear fusion [?] - the creation of an artificial Sun by melting together atomic
76 cores - the virtually inexhaustible and clean source of energy. The oil and gas are limited and unevenly
77 distributed resources, wind does not always blow, the Sun does not shine at night, the wild Nature is still
78 unpredictable and the extracted energy has to be stored in order to level out its production and consumption.

79

80 With the rise of the technological era, over the last century, energy has been delivered to our homes in
81 form of electricity. Energy storage systems such as fuel cells, supercapacitors and batteries are crucial ele-
82 ments for powering portable electronics and vehicles, or for balancing a power grid with a renewable energy
83 source. [16]. Two opposite electric charges separated from each other can store energy in an electrostatic
84 field. It is possible to accumulate many charges on the plates of a capacitor and store some energy [?], but
85 due to the technological difficulties, electrochemical cells are commonly used instead. An electrochemical
86 cell is an energy storage device and a power source that undergoes a chemical reaction to transfer some
87 electric charge from one of its components to another through an external circuit. A simple electrochemical
88 cell consists of three elements: two spatially separated materials called electrodes, and a solution of mobile
89 ions between them called electrolyte. The two electrodes have different work functions, or, chemically
90 speaking, reduction-oxidation (redox) potentials. When the electrodes of the cell are connected through
91 an external circuit, the electrons flow through the circuit and the ions in the electrolyte rearrange to main-
92 tain charge balance [33]. While the cell delivers the electric current to the circuit, a chemical reaction is
93 happening on its electrodes: the positively charged electrode, called cathode, is being reduced, obtaining
94 electrons from the negatively charged anode through the external circuit. The anode loses electrons and
95 is being oxidized. If the electrodes can undergo a reversible redox reaction, a current applied to the cell
96 restores its charged state. The speed, reversibility, released by-products and physical conditions of this
97 redox reaction are the key factors that define the charging rate, cycling stability, the self-discharge rate and
98 the area of application of an electrochemical cell. This type of redox reaction had been of great interest
99 for the field of energy storage, particularly, electrochemistry [?], where numerous characterization tech-
100 niques have been developed to optimize the architecture of electrochemical power sources. Depending on
101 the redox potentials of the used electrodes, the output voltage of a cell ranges between 0 and 5 V. Most
102 applications require higher voltages, so multiple cells are connected in series to form a battery.

103

104 Stable, capacious and powerful batteries have become of great demand for today's energy driven so-
105 ciety [54, 53, 38]. The advances in lithium ion technology for rechargeable batteries have enabled en-
106 ergy densities that make it possible to battery-power a wearable Internet-of-things device [26, 30], an
107 airplane [20] or a house [4, 14]. Still, the application of lithium ion batteries is limited by irreversible
108 processes [25, 8, 58] that occur upon extreme operating conditions such as high power demand [57, 12]
109 or over-discharge [29]. Such degradation processes limit the performance of a battery by lowering its safe
110 operating power, resulting in lower power density and longer charging times. The challenge to overcome
111 these limitations, together with low abundance of Lithium, Cobalt and rare earth metals, [53, 16] and the
112 toxicity of the manufacturing process [41, 39] is motivating research and development of advanced battery
113 technologies [3]. This requires understanding of charge transport and degradation pathways in energy stor-
114 age materials as well as exploring novel materials such as materials based on organic precursors [28, 21].

115 The flexible molecular design together with questions regarding unresolved charge transport- and per-
116 formance limiting mechanisms have inspired a variety of characterization techniques to be developed and
117 applied to both energy storage materials and energy storage devices, operando and ex-situ. Together
118 with electrochemical characterization as the standard method for studying the properties of energy stor-
119 age materials[48, 56], operando optical microscopy [32], neutron imaging [29] and X-ray diffraction [42]
120 were applied to monitor irreversible structural deformations during extreme charging of Li cells.

121 UV and IR spectroscopy turned out to be particularly useful for studying organic energy-storage ma-
122 terials. For instance, it was possible to observe formation of positive polarons in the NiSalen backbone
123 of the pDiTBuS upon its oxidation [5]. Since the electrochemical processes happen within the bulk of
124 the energy storage material and involve changes in the spin states, imaging techniques based on mag-
125 netic resonance can be applied to obtain structural information on the battery electrodes on the molecular
126 level [36, 31, 27, 1]. NMR was used to study dendrite formation, electrolyte dynamics and intercalation of
127 Li ions[24, 11] in Li cells, including operando imaging [47].

128 Operando continuous-wave EPR (cwEPR) was applied to study redox kinetics of inorganic battery
129 cathodes [35], radical formation and spin densities in redox polymers [5] and in organic electrochemical
130 cells [15, 22].

131 Pulsed EPR (pEPR) provides an even more powerful toolbox for material studies with the electron spin
132 as a microscopic structural probe. In particular, pEPR provides access to the dipolar coupling between
133 neighboring electron spins and thus the possibility to determine distances between adjacent redox-active
134 centers using dipolar spectroscopy [43] as in spin-labelled proteins [19, 49]. In addition, the hyperfine
135 coupling between electron and nuclear spins in close vicinity can be measured by electron spin echo en-
136 velope modulation (ESEEM) and electron nuclear double resonance (ENDOR) techniques and can thus
137 elucidate the degree of delocalization for charge carriers in ORB materials in a similar way as in organic
138 semiconductors [6].

139 **EDMR** is allowing to manipulate the spin of an electron that tunnels through a disordered media such as
140 the amorphous silicon in a solar cell, through intertwined fragments of conjugated polymers in an organic
141 solar cell or an organic field-effect transistor.

142

¹⁴³ **Chapter 2**

¹⁴⁴ **Electrochemical Energy Storage in
Redox Conductive Polymers**

¹⁴⁶ **2.1 Redox Conductive Polymers**

¹⁴⁷ A π - conjugated network, such as polyacetylene, exhibits a band structure in the electron energy levels and
¹⁴⁸ represents a molecular semiconductor.

¹⁴⁹ After the discovery of the conductivity of polyacetylene by XXXXX in 1970s, [] the field of organic
¹⁵⁰ electronics has expanded dramatically. Organic solar cells and organic field effect transistors contain con-
¹⁵¹ jugated polymers that have electrical properties of semiconductors, yet can be easily printed in form of thin
¹⁵² flexible films without using high temperatures.

¹⁵³ **2.2 Organic Radical Battery**

¹⁵⁴ Batteries based on conjugated polymers containing stable radical moieties as high-capacitance groups rep-
¹⁵⁵ resent a promising class of future electrochemical power sources - organic radical batteries (ORB) [34, ?, ?,
¹⁵⁶ ?]. ORB combine the advantages of high-power supercapacitors, namely high discharge rates, and the high
¹⁵⁷ energy density of conventional lithium-ion technology. In contrast to the lithium-ion battery, the charging
¹⁵⁸ of an organic battery does not involve intercalation of metal ions into the electrodes. This reduces the struc-
¹⁵⁹ tural change of the electrode upon repeated recharging which allows for a longer cycle life of an ORB. The
¹⁶⁰ semi-conducting nature of organic electrodes reduces the Joule heating during the battery operation, and
¹⁶¹ this allows for higher charge/discharge rates. The amorphous and swollen structure of organic electrodes
¹⁶² allows the electrolyte ions to diffuse faster into the electrode, which also increases the charge/discharge
¹⁶³ rate [37]. A further beneficial property of organic materials over traditional inorganic materials is their
¹⁶⁴ availability and the low cost of the starting materials for the synthesis of the target polymers in conjunction
¹⁶⁵ with good mechanical properties [16, 33, 7]. The large knowledge base on polymer processing allows for
¹⁶⁶ inkjet printing, roll-to-roll processing and other low-cost manufacturing techniques for making low-cost,
¹⁶⁷ flexible and light-weight integrated devices, including flexible plastic batteries [16, 37].

¹⁶⁸ **Organic Electrode Materials**

¹⁶⁹ ORB based on redox polymers containing stable radicals [34] have been shown to compete with or even
¹⁷⁰ outperform conventional Li based batteries in terms of power densities [48] with the additional benefit of
¹⁷¹ being free from rare precursors, inheriting mechanical properties of plastics and electrical properties of
¹⁷² semiconductors [7, 2, 10]. Advanced molecular design techniques allow for tuning of the electrochemical
¹⁷³ properties of the redox polymers [17], that brings in a rich variety of organic energy storage materials [52,
¹⁷⁴ 51, 18] and creates a large room for their optimization.

¹⁷⁵ While active electrode materials with nitroxide radicals as redox-active groups are ideally suited for
¹⁷⁶ organic radical batteries (ORBs) that exhibit high power densities, the broad application of most nitroxide-

based materials is limited by their moderate electrical properties. A promising route towards overcoming the conductivity problem is the use of polymers that combine radical-containing moieties and a conductive backbone. This strategy was successfully followed in a number of studies focusing on different polymers.[?, ?, ?, ?, ?, ?]

2.3 TEMPO-Salen Cathode Material

Redox conductive conjugated polymers containing TEMPO (2,2,6,6-tetramethylpiperidine-1-oxyl) redox groups, as pDiTBuS (poly-di-TEMPO-Butyl-Salen) shown in Figure 2.1, demonstrate particularly promising energy and power densities [50]. The pDiTBuS was designed as a cathode material: it is oxidized when the electrochemical cell containing this material is charged. A film of pDiTBuS comprises a high concentration of redox active stable nitroxyl radicals attached to a conjugated polymer backbone that interconnects them as a molecular wire. Such system may be viewed as a highly disordered molecular hole-transporting semiconductor (the poly-NiSalen backbone) that contains a large amount of hole traps (TEMPO groups) attached to it with butyl linkers. When the film is reduced (discharged), the TEMPO groups are in the radical state and act as unfilled traps. Upon oxidation (charging), the TEMPO fragments lose an unpaired electron and acquire a positive charge, so the traps are being filled with holes.

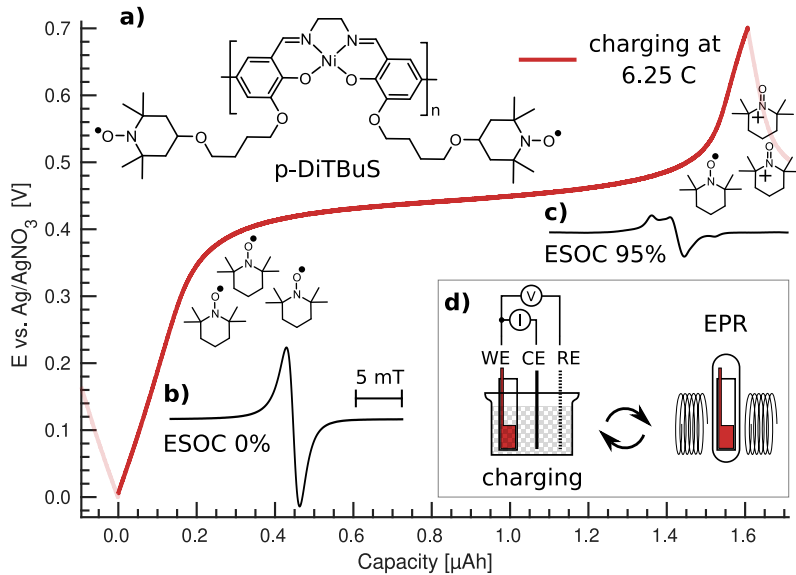


Figure 2.1: Galvanostatic charge-discharge curve for a pDiTBuS cathode film at 10 μ A (6.25 C), chemical structure of pDiTBuS (a), normalized cwEPR spectral signatures for reduced (b) and oxidized (c) states. Scheme of the ex-situ EPR measurement on the pDiTBuS half cell (d).

¹⁹² **Chapter 3**

¹⁹³ **Operando EPR Spectroscopy of
194 TEMPO-Salen Cathode Films**

¹⁹⁵ **3.1 Electron Paramagnetic Resonance**

¹⁹⁶ **3.1.1 The Spin Hamiltonian**

¹⁹⁷ **Electron Spin** In the Poincaré group of special relativity [40], when relativistic boosts and rotations
¹⁹⁸ are considered, there emerges an additional quantity that is preserved together with the orbital angular
¹⁹⁹ momentum, yet it is retained for point objects - spin [23]. Spin is quantized, it can take values in integer-
²⁰⁰ or half-integer multiples of the Planck's quantum of action \hbar up to a certain magnitude S . The electron,
²⁰¹ as a fundamental particle and a fermion, bears a half-integer spin with a magnitude of $S = 1/2$. Spin
²⁰² combines with the charge of the electron to endow the electron with a magnetic moment $\mu_{\text{spin}}^{\rightarrow} = \gamma \vec{S}$, where
²⁰³ $\gamma = \frac{g_e \mu_B}{\hbar} \approx 28.025 \text{ GHz/T}$ is the gyromagnetic ratio of the electron, $\mu_B = \hbar e/m_e$ is the Bohr magneton
²⁰⁴ and $g_e \approx 2.00231930$ is the electron g factor. The magnetic moment of the electron is quantized [9]: the
²⁰⁵ eigenvalues of the spin operator for the electron \vec{S} take only two half-integer values $\pm \frac{\hbar}{2}$.

²⁰⁶ When an electron is placed in a static magnetic field $\vec{B}_0 = B_0 \vec{e}_z$, its magnetic moment precesses about
²⁰⁷ the field direction with the Larmor frequency $\omega_L = \gamma B_0$. The projection of the electron spin on the direction
²⁰⁸ of the magnetic field can take only discrete values between $-S = -1/2$ and $S = 1/2$, so that the eigenvalues
²⁰⁹ of the z component of the spin operator are also discrete:

$$\begin{aligned}\hat{S}_Z |\uparrow\rangle &= +\frac{\hbar}{2} |\uparrow\rangle \\ \hat{S}_Z |\downarrow\rangle &= -\frac{\hbar}{2} |\downarrow\rangle\end{aligned}\tag{3.1}$$

²¹⁰ The two eigenfunctions of \hat{S}_Z are called the spin-up state $|\uparrow\rangle$ and the spin-down state $|\downarrow\rangle$. The two
²¹¹ corresponding eigenvalues $\pm \frac{\hbar}{2}$ define the energy difference between the states $|\uparrow\rangle$ and $|\downarrow\rangle$, that is known as
²¹² the Zeeman splitting. Depending on the effects that are relevant for the local environment of the electron,
²¹³ its Hamiltonian contains a number of terms, each corresponding to a certain type of interaction.

²¹⁴ **Zeeman Splitting** The energy of a free electron placed in the external magnetic field \vec{B}_0 is the eigen-
²¹⁵ value of the spin Zeeman Hamiltonian: $\hat{H}_{EZ} = \frac{\mu_B}{\hbar} g_e \vec{B}_0 \cdot \vec{S}$. In the laboratory frame of reference $\vec{B}_0 \parallel \vec{e}_z$,
²¹⁶ $[\hat{H}_{EZ}, \hat{S}_z] = 0$, so \hat{H}_{EZ} and \hat{S}_Z share the two eigenfunctions $|\uparrow\rangle$ and $|\downarrow\rangle$. The Zeeman energies of the elec-
²¹⁷ tron are $E_{EZ}^{\pm} = \pm \frac{1}{2} \mu_B g_e B_0$, their difference defines the magnitude of the electron Zeeman splitting at a given
²¹⁸ magnetic field:

$$\Delta E_{EZ} = \mu_B g_e B_0\tag{3.2}$$

Nuclear Spin and Nuclear Zeeman Splitting A proton has a half-integer spin $S = 1/2$ that results in a magnetic moment $\mu_p = \mu_e \frac{m_e}{m_p}$, that is $\frac{m_e}{m_p} \approx 1836$ times smaller than the electron's magnetic moment. A neutron bears no charge but also has a half-integer spin $S = 1/2$. An atomic nucleus that consists of protons and neutrons has a magnetic moment which is a vector sum of the aligned spins of its protons and neutrons (nucleons). The spin of a nucleus is defined by the arrangement of its nucleons and on the nuclear charge. A nitrogen nucleus has 7 protons and 7 neutrons that total in a nuclear spin $I = 1$ which, with the g factor for the nitrogen nucleus g_N , results in the nuclear magnetic moment of $\mu_N = \mu_B g_N \frac{m_e}{m_N} I$ that splits into three Zeeman energy levels corresponding to the three possible projections of the nuclear spin on the magnetic field axis, $m_I = -1, 0, +1$, analogously to the electron with $m_S = 1/2, -1/2$. The nuclear Zeeman splitting is more than two orders of magnitude weaker than the electron Zeeman splitting because of the difference in the masses of the particles.

Hyperfine Interaction The magnetic moments of an electron and a magnetic nucleus, such as nitrogen, couple in the hyperfine interaction [45]: $H_{HF} = \vec{S} \vec{A} \vec{I} = H_F + H_{DD}$ with the hyperfine coupling tensor **A**. The isotropic part $H_F = a_{iso} \vec{S} \vec{I}$, or the Fermi contact interaction, scales with the probability density of the electron at the position of the nucleus $a_{iso} = \frac{2}{3} \frac{\mu_0}{\hbar} g_e \mu_e g_N \mu_n |\psi(0)|^2$. The anisotropic part $H_{DD} = \vec{S} \vec{T} \vec{I}$ with the dipolar coupling tensor **T** takes into account the anisotropic dipole-dipole coupling between the magnetic moments of the electron and the nucleus.

Nuclear Quadrupole Moment The nitrogen nucleus has a spin greater than 1/2 which alters the charge distribution within the nucleus which gives rise to a non-vanishing nuclear electrical quadrupole moment Q . The interaction between the asymmetrically distributed charge and the gradient of the electric field at the nucleus is given by the nuclear quadrupole Hamiltonian $H_{NQ} = \vec{I} \vec{P} \vec{I}$ with the nuclear quadrupole tensor **P** that describes the coupling of the nuclear quadrupole moment to the electric field gradient.

Exchange Interaction In a system of closely placed electrons, such as in a film of densely packed nitroxide radicals, the electron orbitals may overlap significantly and the radicals may exchange electrons. The energy required to exchange the electrons is called the Heisenberg exchange coupling $H_{exch} = \vec{S}_1 \vec{J} \vec{S}_2$, that becomes considerably large at inter-spin distances below $r < 1.5$ nm or with a large spin delocalization [46]. The positive **J** corresponds to a weak coupling between S_1 and S_2 which leads to an antiferromagnetic or antiparallel alignment of spins with a total $S = 0$, whereas the negative **J** causes the strong inter-spin coupling which leads to a ferromagnetic alignment with $S = 1$.

Magnetic Dipole-Dipole Interaction The dipole-dipole interaction between the two neighboring electron spins contributes one more term to the spin Hamiltonian: $H_{dd} = \vec{S}_1 \vec{D} \vec{S}_2$ that depends on the distance between the spins.

The Spin Hamiltonian For the interactions considered in this thesis, the following Hamiltonian will be applied to describe the interactions of unpaired electron spins with their local environments, ranging by their magnitude:

$$H = H_{EZ} + H_{HF} + H_J + H_{NZ} + H_{dd} + H_{NQ} = \quad (3.3)$$

The electron Zeeman term H_{EZ} defines the requirements on the hardware and sets the range of the magnetic fields used in the spectroscopic experiments. The hyperfine interaction term H_{HF} allows for reconstruction of the hyperfine coupling tensor from the recorded spectra which is used as a marker to identify the molecular structure and dynamics of the mobile molecular fragments in an electrochemical cell in Section ???. The exchange interaction term H_J and the dipole-dipole interaction term H_{dd} will be used to characterize the packing of the molecular fragments in the cathode film. The nuclear quadrupole interaction term will be used to speculate on the unusual peak intensities in the cryogenic pulsed EPR spectra of charged films in Section ??.

262 **3.1.2 Instrumentation**

263 **cwEPR Hardware** First observed in 1944 [55, 44], the phenomenon of electron paramagnetic resonance
 264 had become a tool for probing local molecular environments in species that contain unpaired electron
 265 spins. A free electron, that does not interact with its environment and has $g = g_e$, experiences a Zeeman
 266 splitting of $\Delta E = g\mu_B B_0$, that corresponds to the energy of a photon with a frequency of $\nu = \Delta E/h$. At
 267 $B_0 \approx 0.3$ T, a microwave photon with $\nu \approx 9.5$ GHz (IEEE X band, $\nu = 8 - 12$ GHz, $\lambda = 2.5 - 3.8$ cm) can
 268 drive the magnetic dipole transition between $|\uparrow\rangle$ and $|\downarrow\rangle$ - that is called the spin flip. In a simple cwEPR
 269 experiment, the frequency and power of the microwave source is kept constant and the magnetic field is
 270 scanned around the values given by the Eq. 3.2. and the microwave absorption is observed as a function
 271 of the magnetic field. The allowed spin transitions are manifesting themselves as peaks in the microwave
 272 absorption coefficient when recorded with respect to the magnetic field. More advanced methods that
 273 involve coherent spin dynamics and pulsed microwave fields are discussed in Chapter 4.

274 A basic cwEPR spectrometer consists of a magnet, a microwave source, a resonator and a detector.
 Figure 3.1 depicts those elements with more details.

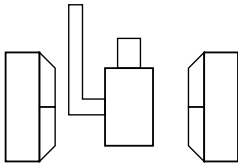


Figure 3.1: Diagram of a cwEPR spectrometer

275 To ensure that only the magnetic component of the microwave photon is interacting with the sample,
 276 a standing microwave is formed in a resonating cavity with a resonance frequency close to that of the
 277 microwave source. In the center of the cavity, the magnetic component of the microwave is maximized and
 278 the electric component is quenched. When the sample is inserted in the center of the cavity, it is mostly
 279 the magnetic component of the microwave that is interacting with it. That allows one to drive a magnetic
 280 dipole transition without heating up the sample. A sample of finite dimension, especially if it contains
 281 metals, changes the distribution of the microwave field inside the cavity, shifts the resonance frequency of
 282 the cavity and changes its quality factor Q . The frequency of the microwave source is adjusted so that it
 283 fits the new eigenmode of the cavity.

284 and the external magnetic field is swept. When the resonance condition is met ??, the spin flip occurs
 285 and the photon is being absorbed by the sample. The resonance absorption of microwaves can be detected
 286 by a small decrease in the quality factor Q of the resonating cavity, as the magnetic field is being scanned
 287 and the microwave frequency is kept constant. The change in the Q factor during the spin flip leads to
 288 temporal decoupling of the resonator, that causes reflections of the microwave that would have entered the
 289 resonator off resonance. The intensity of the microwaves is measured with a biased semiconductor diode
 290 that has a linearly changing conductivity in the range corresponding to the incident microwave power. A
 291 phase sensitive detection with the shallow modulation of B_0 increases the signal-to-noise ratio (SNR), and
 292 yields the derivative of the resonance absorption profile. The typically high $Q \gg 1$ factor of the resonating
 293 cavity further increases the SNR.

295 **3.2 EPR Spectroscopy of a Charging Electrochemical Cell**

296 There is a number of difficulties when it comes to an EPR experiment on a working electrochemical cell.
 297 The cell must contain mobile ions between its electrodes - cations and anions. The ions are normally

produced as products of dissociating salts. To overcome the ionic bond in a salt and to break it into the ions, a solvent with large dipole moment is needed. Solvents with large dipole moments, as acetonitrile (CH_3CN , $\epsilon \approx 37.5$) or water ($\epsilon \approx 78.4$), have large dielectric constants which results in a non-resonant absorption of microwaves. A cell containing liquid electrolyte absorbs microwaves and lowers the sensitivity of the EPR experiment. Furthermore, due to a finite dimension of cell, not only the magnetic component of the microwave is interacting with the electrolyte, but also the electric one - this results in heating of the electrolyte in a similar fashion as in a microwave oven. The heating of the electrolyte leads to a faster degradation of the cell and does not allow for long systematic measurements.

Another general issue with the operando EPR and EDMR experiments is that the device under testing (DUT) has to have metal electrodes that deliver current to it. Metals, placed in a microwave cavity, change the distribution of the electromagnetic field in it - that weakens the magnetic component at the device and at the same time strengthens the electric component. It is the magnetic dipole transition that is causing the magnetic resonance, so the weakening of the magnetic component by introducing the metal electrodes further decreases the magnetic resonance response. The increased electric component causes heating to temperatures that can be critical for the DUT operation.

3.2.1 Fabrication of EPR-compatible Electrochemical Cells

3.2.2 cwEPR Spectra During a Charge-Discharge Cycle

There are four characteristic cwEPR signatures of an electrochemical cell containing di-TEMPO-Salen polymer cathode. The well known signature of a freely tumbling TEMPO[•] exhibits three narrow lines corresponding to the three nuclear sublevels of nitrogen: $m_I = -1, 0, +1$.

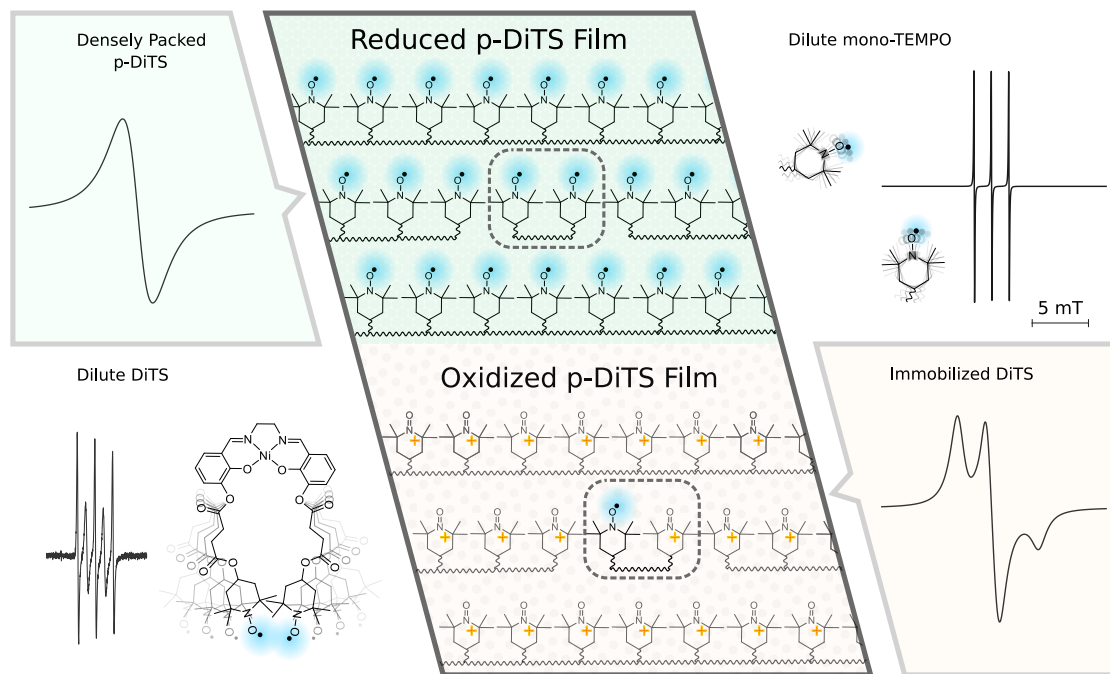


Figure 3.2: XXX

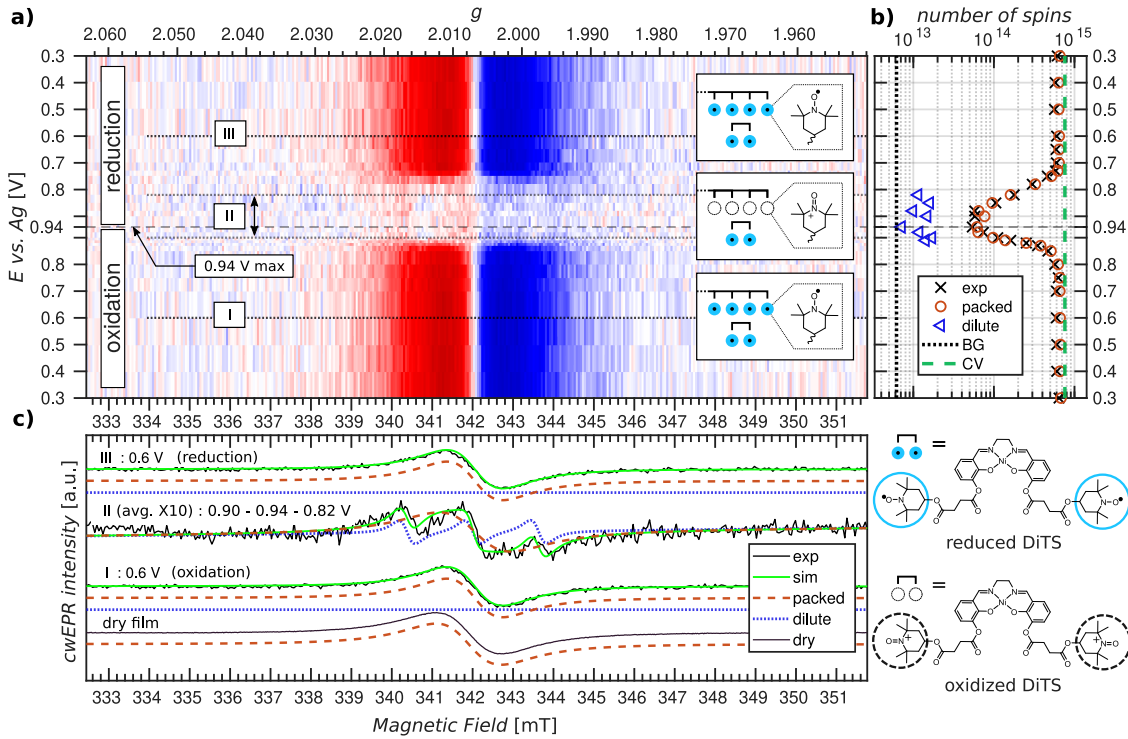


Figure 3.3: XXX

3.2.3 Spectral Simulations

3.2.4 Quantitative Analysis of Potential-Dependent EPR Spectra

3.2.5 EPR-Detected State Of Charge

3.2.6 Formation of Singlet Spin States in a Reduced Cathode Film

3.2.7 Monitoring of Degradation Processes

3.2.8 Monitoring of Self Discharge

Organic Radical Batteries have a tendency to self-discharge, as the organic electrochemically active layer partially dissolves in polar electrolytes. Particularly for the TEMPO containing ORB, the dissolved, mobile TEMPO fragments serve as redox shuttles that carry the charge between the battery electrodes and cause a self discharge. The amount of unoxidized TEMPO[•] shuttles can be measured with cwEPR spectroscopy as the mobile fragments have distinct spectra as compared to the fragments tightly packed in the electrode. Further in this subsection operando spectra of a TEMPO containing electrochemical cells are shown. Quantitative analysis of the released fragments during a charge-discharge cycle allows for a description of the self-discharge process in an ORB. The charge state of a battery is monitored with cwEPR and, additionally, with a potentiometric measurement to identify the self-discharge rate and to connect it with the concentration of diffusing redox shuttles.

3.2.9 Electrochemical Cells with Solid Electrolyte

3.2.10 Low Temperature Measurements

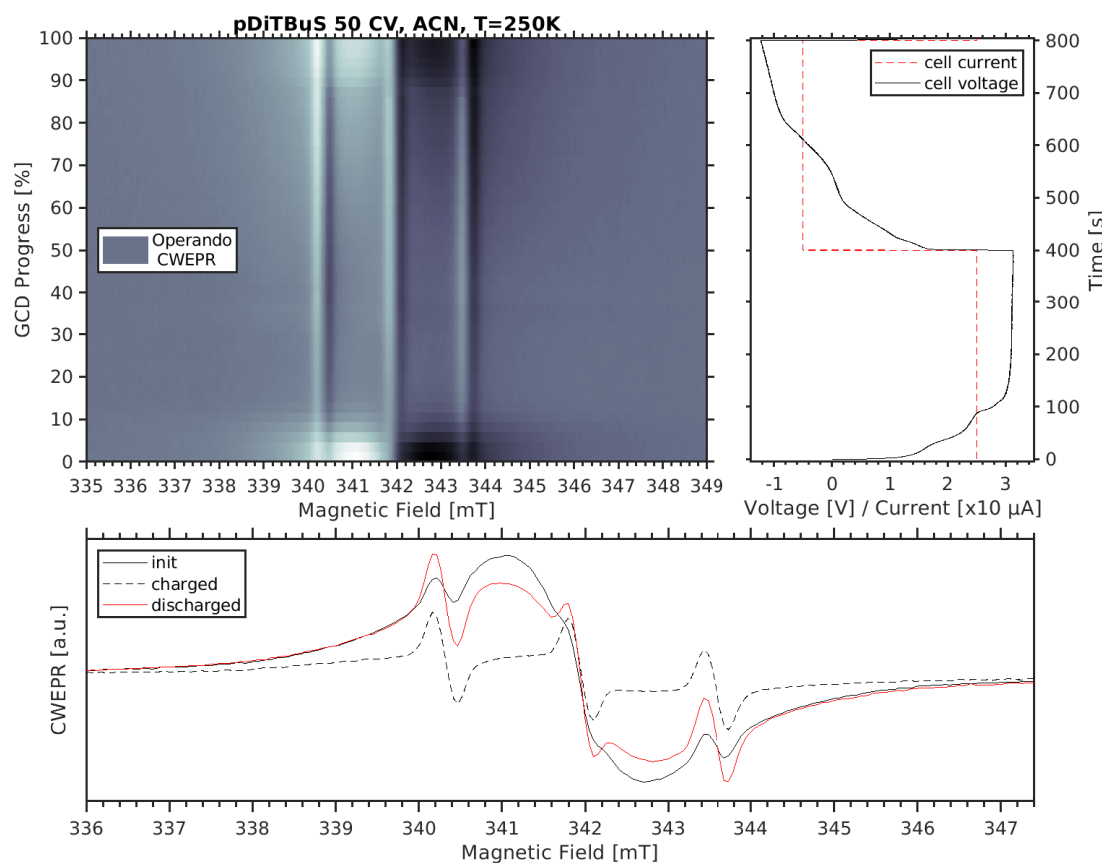


Figure 3.4: XXX

336

Chapter 4

337

pEPR Spectroscopy of Densely Packed Nitroxide Radicals

338

339

4.1 Coherent Spin Motion under Pulsed Microwave Field

340

When a spin system is excited with a microwave pulse, its evolution is described with the set of equations that is known as the Bloch equations.

341

342

4.1.1 Bloch Equations

343

4.1.2 Spin Relaxation Times

344

4.1.3 Spin Packets

345

4.2 Instrumentation

346

4.2.1 Pulse Sequences and Measurement Techniques

347

The Refocused Spin Echo

348

The Hahn Echo sequence consists of two pulses, the $\pi/2$ pulse and the π pulse, separated in time by τ : $\pi/2 - \tau - \pi - \tau - echo$. Initially, the macroscopic magnetization of the spin system is aligned along \vec{B}_0 : $\vec{M}_0 = M_Z \vec{e}_Z$. The $\pi/2$ microwave pulse has such length $t_{\pi/2}$ and amplitude B_1 that, during the pulse, \vec{M} nutates to the xy plane, where it keeps precessing about \vec{e}_Z after the end of the pulse. The difference in local environments for each individual spins in the spin packet, as well as the interactions between the spins, that make up \vec{M} , leads to slightly different precession frequencies ω_L^i of the spins. After some time τ , the difference in the precession frequencies translates into the differences in phases so that the vector sum of the excited spins averages down to $\vec{0}$ for sufficiently long τ . In other words, the excited spin packet dephases with time. The dephasing due to different local spin environments can be reversible if the deviations of the precession frequencies do not depend on time, as is the case for separated electrons in an inhomogeneous solid. In such case, a π pulse can be applied to the spin system to flip every single spin in the dephased spin packet by 180deg in a plane containing \vec{e}_Z , so that the spins keep precessing in the xy plane, but the direction of precession is inverted for them, leading to the effect that is opposite to the initial dephasing. So a τ after the π pulse excites the spin packet, the accumulated phase differences become the smallest and the packet recovers its macroscopic magnetization \vec{M} that oscillates in the xy plane with $\langle \omega_L^i \rangle$ and can be detected. The recovered \vec{M} at $t = \tau$ after the π pulse is called the refocused spin echo. The difference in ω_L^i leads to a further dephasing of the considered spin packet and to the vanishing of \vec{M} .

365

366 **Spin Echo Decay and Phase Memory Time**

367 **Inversion Recovery and Spin-Lattice Relaxation Time**

368 **4.2.2 Broad-Band Excitation and Instantaneous Diffusion**

369 In Section /// it is shown that in a densely packed radical system, as in a TEMPO-Salen cathode film, the
 370 phase memory time can be shorter than $T_m \leq 100$ ns. That is, the spin echo is decaying by $e \approx 3$ at
 371 $t = 100$ ns. The short phase memory time limits the duration of the pulse sequence at which the echo is
 372 detectable. For a $\pi/2 - \tau - \pi - \tau - \text{echo}$ sequence, with a hardware limitation on $\tau \geq t_d \approx 100$ ns, the pulse
 373 sequence is longer than $t > 200$ ns. By this time, the spin echo decreases by $e^2 \approx 7$ and may be comparable
 374 to noise. The limitations imposed by the finite T_m and t_d force one to use shorter microwave pulses.

375 A short microwave pulse may have a spectral width comparable to the width of the observed spectrum.
 376 According to the Fourier theorem, the spectral width of a pulse is inversely proportional to the pulse length:
 377 $\Delta\omega \sim 1/t_p$. A spectrum of a 100 ns long rectangular pulse shown in Figure /// is ///MHz wide (FWHM).

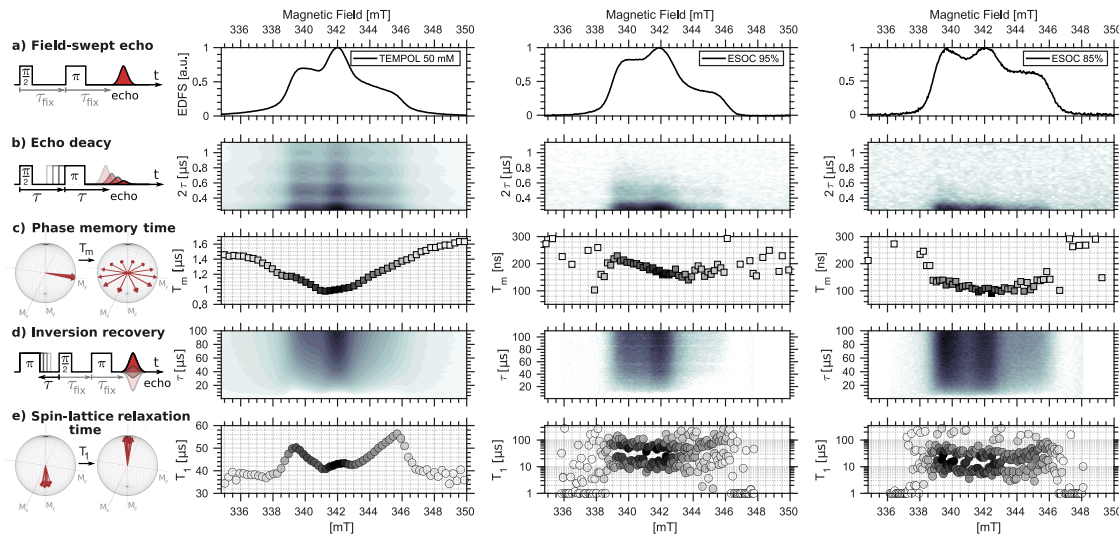


Figure 4.1: XXX

378 **4.3 Pulsed EPR Spectroscopy of a charged pDiTBuS Cathode film**

379 **4.3.1 Field Swept Echo of a charged pDiTBuS Cathode film**

380 **4.3.2 Estimation of Local Spin Concentrations with Instantaneous Diffusion**

381 **4.3.3 Spin Relaxation in a charged pDiTBuS Cathode Film**

382 **4.4 Padé-Laplace Deconvolution of Polyexponential Decay Signals**

383 The echo decay and inversion recovery transients measured in the corresponding experiments may contain
 384 multiple exponential decay components. The conventional method of determining the distribution of the
 385 decay components in a transient decay is the Laplace inversion, where the signal in the time domain $s(t)$ is
 386 converted into its Laplace image $L(p) = \int_0^{+\infty} s(t)e^{-pt} dt$ in the time-constant domain $p = 1/t$, where the peaks
 387 of $L(p)$ give the decay constants that make up the signal. However, for the noisy signal, the direct calcula-
 388 tion of the Laplace transform brings in artifacts that drastically vary with the noise. The signal-to-noise
 389 ratio (SNR) of the recorded data makes it difficult to apply the Laplace inversion to determine the number

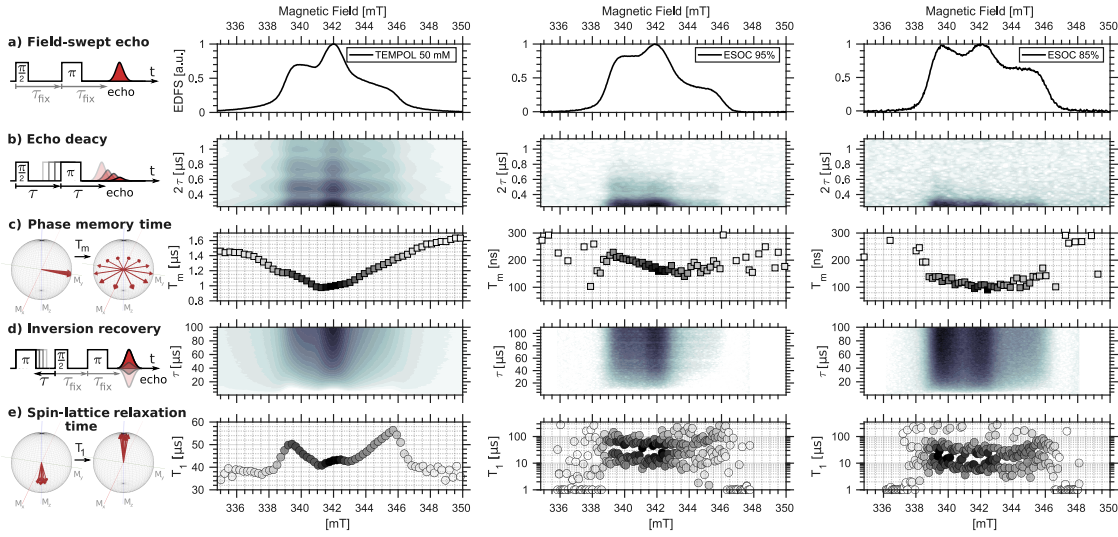


Figure 4.2: XXX

of the decay components, as the Laplace transform is unstable at that SNR.

The Padé-Laplace method comes useful for analyzing noisy polyexponential decays as it was demonstrated in Ref. [13]. The idea of the Padé-Laplace method is to analyze the Padé approximation of the Taylor expansion of the $L(p)$ in the vicinity of one of the expected decay constants p_0 , rather than considering the $L(p)$ fully. This way of signal decomposition is stable against the noise for $\text{SNR} < 10$ (see Figure 4.3). The number of exponents detected by the Padé-Laplace method as well as their locations in the p space may vary depending on the expansion point p_0 . We considered $p_0 = 1/t_{1/2}$ where $t_{1/2}$ is the time at which the signal amplitude halves.

We implemented the following algorithm to detect the number of exponents in the decaying transient $s(t)$:

First, a point $p_0 = 1/t_{1/2}$ was chosen, at which $s(t)$ halves.

Then, 11 coefficients of the Taylor expansion of the Laplace transform $L(p)$ were calculated in the vicinity of $p \rightarrow p_0$

$$L(p)|_{p \rightarrow p_0} = \sum_{n=0}^{11} d_i (p - p_0)^i \quad (4.1)$$

with

$$d_i = \frac{1}{i!} \left(\frac{d^{(i)} L}{dp^{(i)}} \right)_{p=p_0} \quad (4.2)$$

where the derivatives $\frac{d^{(i)} L}{dp^{(i)}}$ are computed numerically at the point $p = p_0$ from the discrete signal $s(t) = (t_j, f_j)$, $j = 1 \dots M$:

$$\frac{d^{(i)} L}{dp^{(i)}} = \sum_{j=2}^{M-1} (-t_j)^i e^{(-p_0 t_j)} f_j + \frac{1}{2} \left((-t_1)^i e^{(-p_0 t_1)} f_1 + (-t_M)^i e^{(-p_0 t_M)} f_M \right) \quad (4.3)$$

Then the Taylor expansion for $L(p)$ was approximated in the vicinity of p_0 with the Padé polynomials $a(p)$ and $b(p)$ of orders $n = 5$ and $n = 6$ respectively:

$$L(p)|_{p \rightarrow p_0} = d_0 + d_1(p - p_0) + \dots + d_{11}(p - p_0)^{11} = \frac{a_0 + a_1(p - p_0) + \dots + a_5(p - p_0)^5}{1 + b_1(p - p_0) + \dots + b_6(p - p_0)^6} \quad (4.4)$$

414 The equation 4.4 is multiplied by the denominator and the prefactors at $(p - p_0)^n$ for $n = 6 \dots 11$
 415 are compared. This defines a system of linear equations on coefficients b_i :

416

$$\begin{pmatrix} d_5 & d_4 & d_3 & d_2 & d_1 & d_0 \\ d_6 & d_5 & d_4 & d_3 & d_2 & d_1 \\ d_7 & d_6 & d_5 & d_4 & d_3 & d_2 \\ d_8 & d_7 & d_6 & d_5 & d_4 & d_3 \\ d_9 & d_8 & d_7 & d_6 & d_5 & d_4 \\ d_{10} & d_9 & d_8 & d_7 & d_6 & d_5 \end{pmatrix} \begin{pmatrix} b_1 \\ b_2 \\ b_3 \\ b_4 \\ b_5 \\ b_6 \end{pmatrix} = \begin{pmatrix} -d_6 \\ -d_7 \\ -d_8 \\ -d_9 \\ -d_{10} \\ -d_{11} \end{pmatrix} \quad (4.5)$$

417

From 4.5, b_i are found. The coefficients a_i are found from d and b .

418

419 Finally, the Padé approximation $P = \frac{a}{b}$ is constructed and its poles are analyzed. The position of
 420 the poles reveal the decay constants. The residues at the poles may give the amplitudes of the decay
 421 components, but this was not used in the present study.

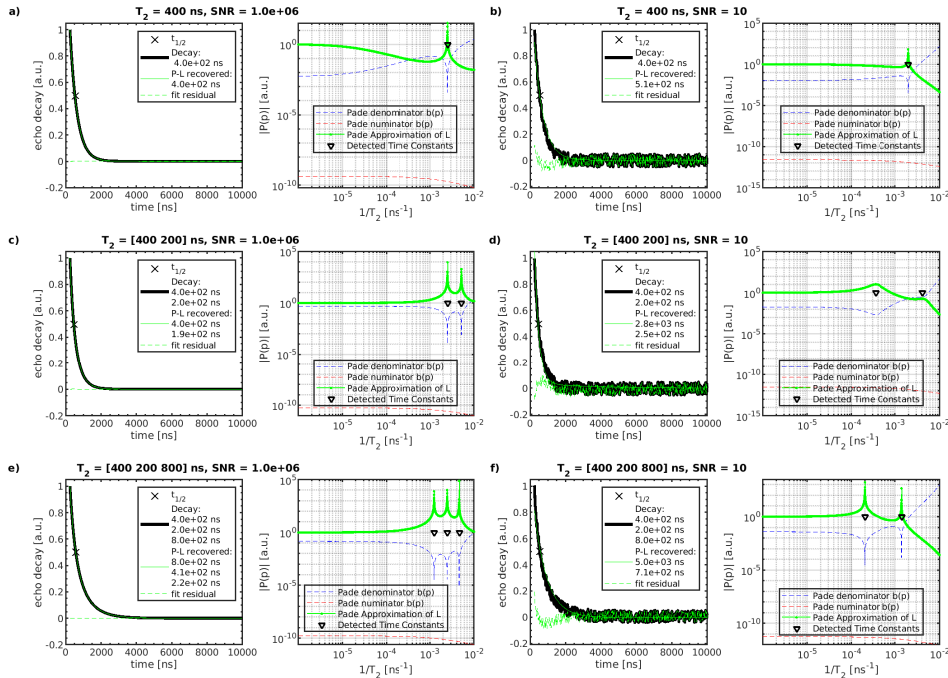


Figure 4.3: Padé-Laplace deconvolution of the mock data containing two decay constants with various signal-to-noise (SNR) ratios.

422 **4.4.1 Padé-Laplace Deconvolution of the Echo-Decay and Inversion-Recovery Tran-**
423 **sients**

424 We used the Padé-Laplace method to determine the number of the decay constants in the signals and used
425 multiexponential fits to adjust the decay constants and their amplitudes. For the echo decay transients the
426 best fits were monoexponential fits, even though the Pade-Laplace analysis initially showed biexponential
427 behavior for pDiTBuS with major contribution from the fast decay constants in the order of the detector's
428 dead time. All recorded echo decay transients contain oscillations due to the ESEEM effect. The oscilla-
429 tions were excluded from the analysis as shown in the 'fit area' on the plots in Figure 4.5, Figure 4.7 and
430 Figure 4.9.

⁴³¹ Echo Decay in 50 mM TEMPOL

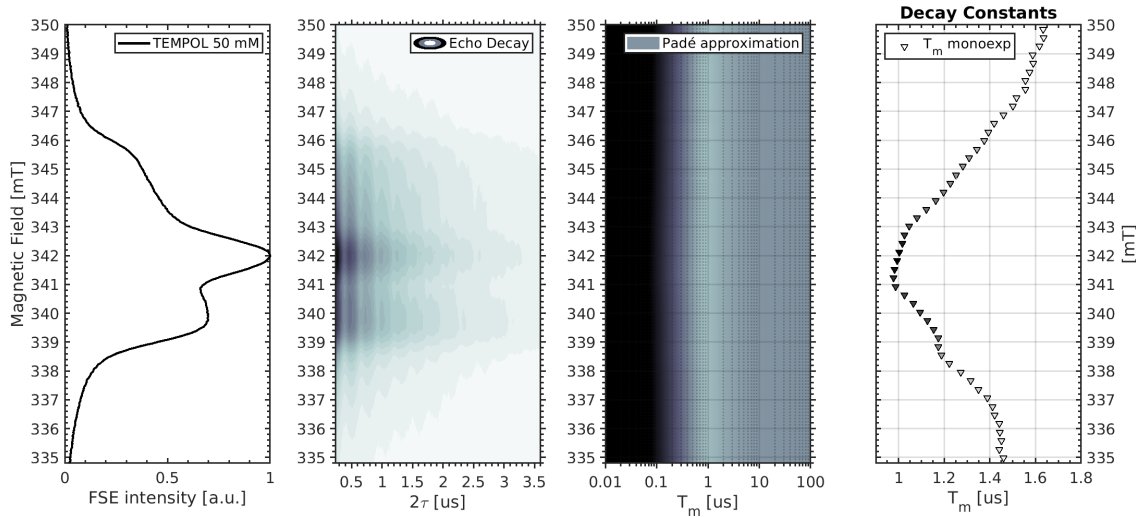


Figure 4.4: Padé-Laplace deconvolution of the field-swept spin echo decay in a frozen 50 mM solution of TEMPOL in Dichloromethane:Acetonitrile glass (3:1). One decay component detected with Padé-Laplace (triangles, right panel). Monoexponential fit (squares for faster component, circles for slower component, right panel). Temperature 5K.

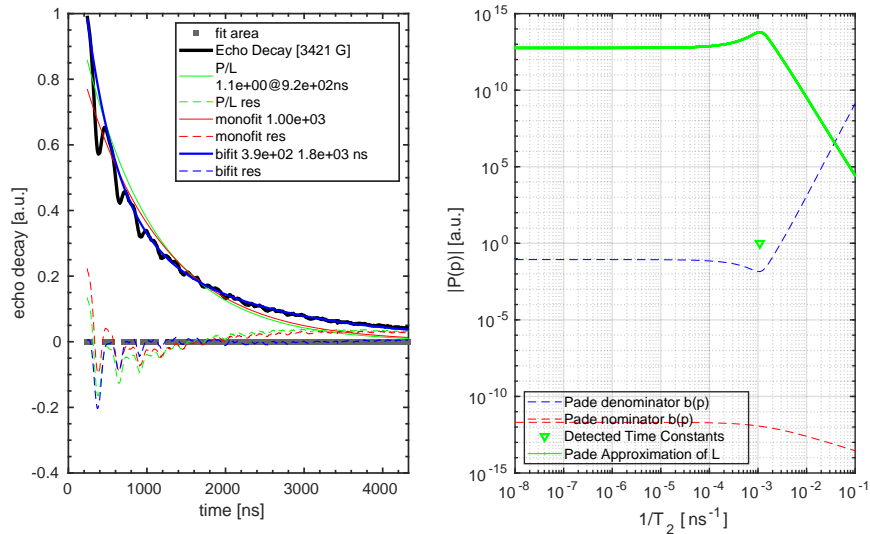


Figure 4.5: Fits of the echo decay transient in the frozen 50 mM TEMPOL solution at the central spectral peak ($m_I = 0$, 342 mT). Padé-Laplace deconvolution the transient vs. free monoexponential fit vs biexponential fit. Temperature 5K. Data was fit in the 'fit area' region. ESEEM oscillations were excluded from the data for fit and Padé-Laplace analysis.

432 Echo Decay in DiTBuS 95% ESOC

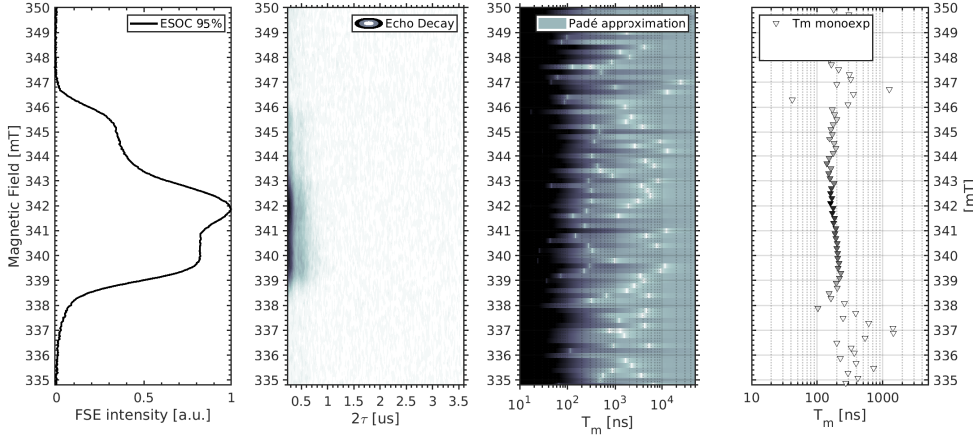


Figure 4.6: Padé-Laplace deconvolution of the field-swept spin echo decay in the pDiTBuS film at 95% ESOC. Temperature 5K.

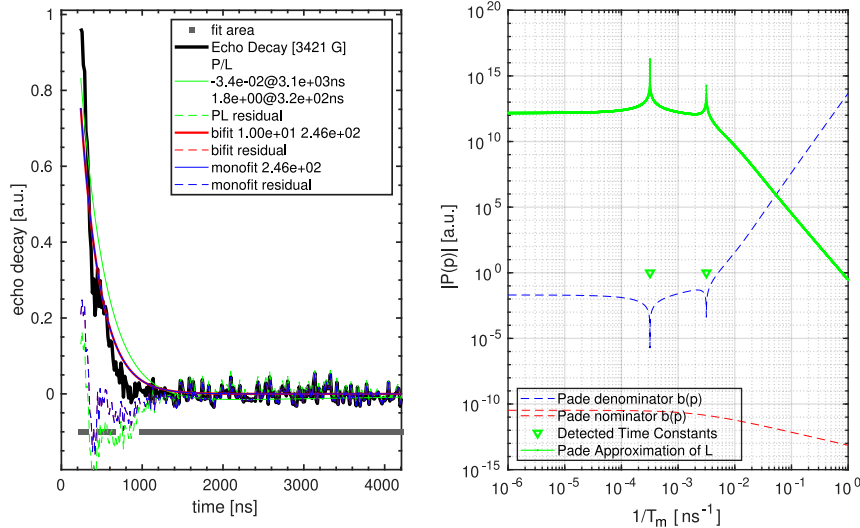


Figure 4.7: Fits of the echo decay transient in the pDiTBuS film at 95% SoC at the central spectral peak ($m_l = 0$, 342 mT). Padé-Laplace deconvolution the transient vs. free monoexponential fit vs biexponential fit. Temperature 5K. Data was fit in the 'fit area' region. ESEEM oscillations were excluded from the data for fit and Padé-Laplace analysis.

433 Echo Decay in DiTBuS 85% ESOC

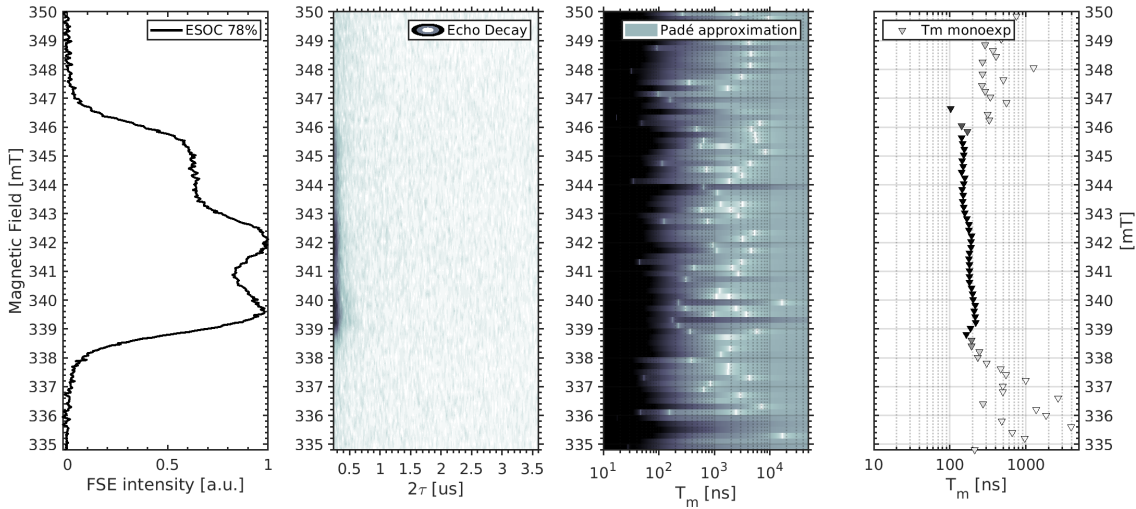


Figure 4.8: Padé-Laplace deconvolution of the field-swept spin echo decay in a pDiTBuS film at 85% SoC. Temperature 5K.

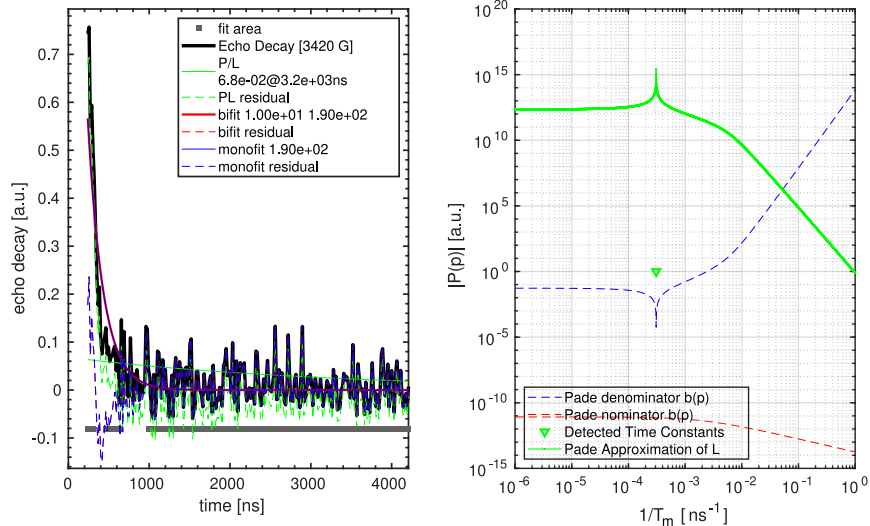


Figure 4.9: Padé-Laplace deconvolution, biexponential and monoexponential fits of the spin echo decay in a pDiTBuS film at 85% SoC at the $m_I = 0$ spectral position. Temperature 5K. Data was fit in the 'fit area' region. ESEEM oscillations were excluded from the data for fit and Padé-Laplace analysis.

434 Inversion Recovery in 50 mM TEMPOL

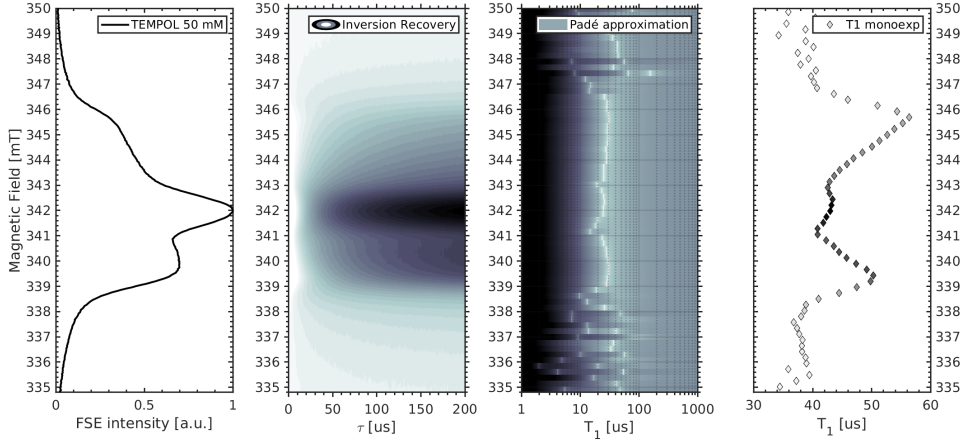


Figure 4.10: Padé-Laplace deconvolution of the field-swept inversion recovery in a frozen 50 mM solution of TEMPOL in the Dichloromethane:Acetonitrile glass (3:1). Two decay components detected with Padé-Laplace (separated poles in the Padé-Laplace approximation, third panel). Biexponential fit (circles for faster component, squares for slower component, right panel). Temperature 5K.

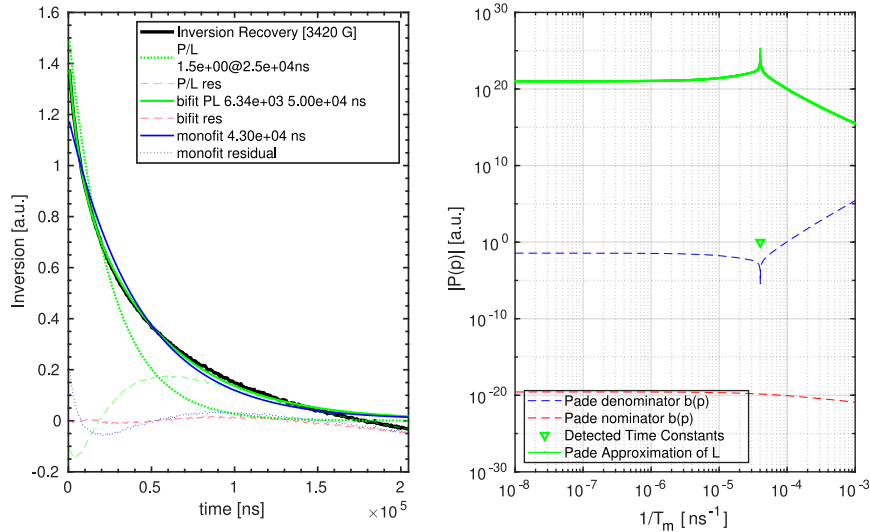


Figure 4.11: Fits of the inversion recovery transient in the frozen 50 mM TEMPOL solution at the central spectral peak ($m_I = 0$, 342 mT). Padé-Laplace deconvolution the transient and a biexponential fit. Temperature 5K.

435 **Inversion Recovery in DiTBuS 95% ESOC**

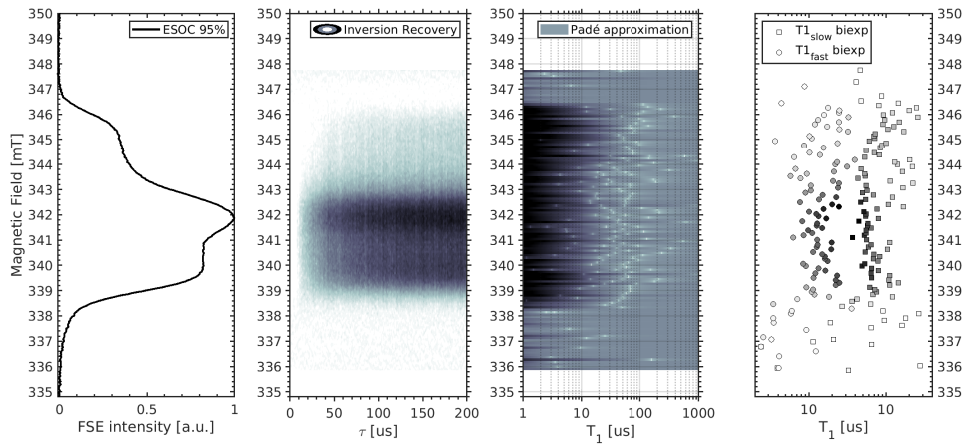


Figure 4.12: Padé-Laplace deconvolution of the field-swept inversion recovery in a pDiTBuS film at 95% ESOC. Temperature 5K.

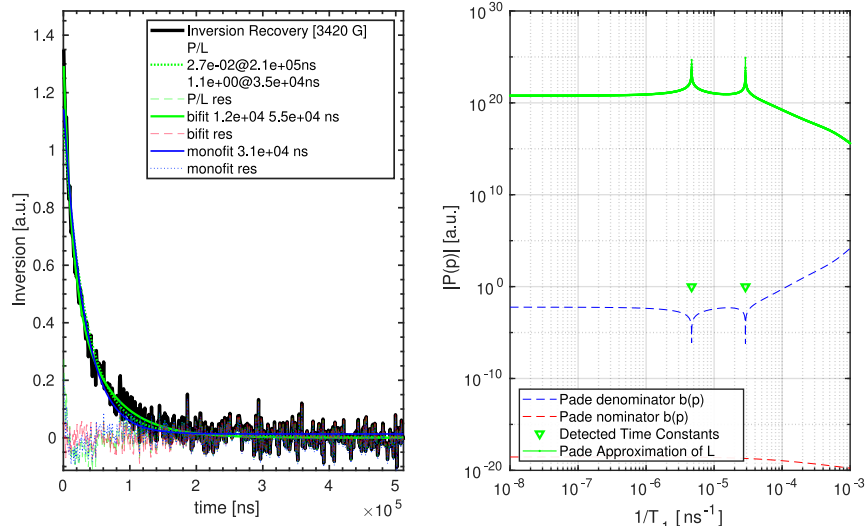


Figure 4.13: Fits of the inversion recovery transient in the 95% ESOC pDiTBuS film at the central spectral peak ($m_I = 0$, 342 mT). Padé-Laplace deconvolution the transient and a biexponential fit. Temperature 5K.

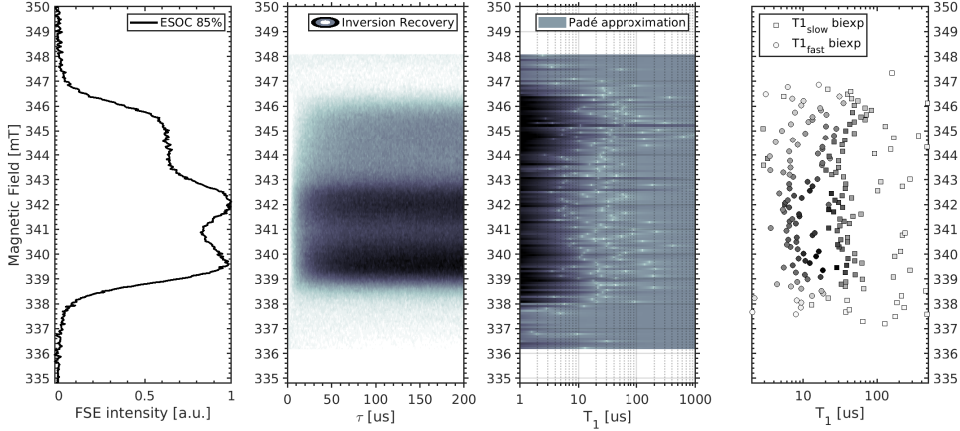
436 **Inversion Recovery in DiTBuS 85% ESOC**

Figure 4.14: Padé-Laplace deconvolution of the field-swept inversion recovery in a pDiTBuS film at 85% ESOC. Temperature 5K.

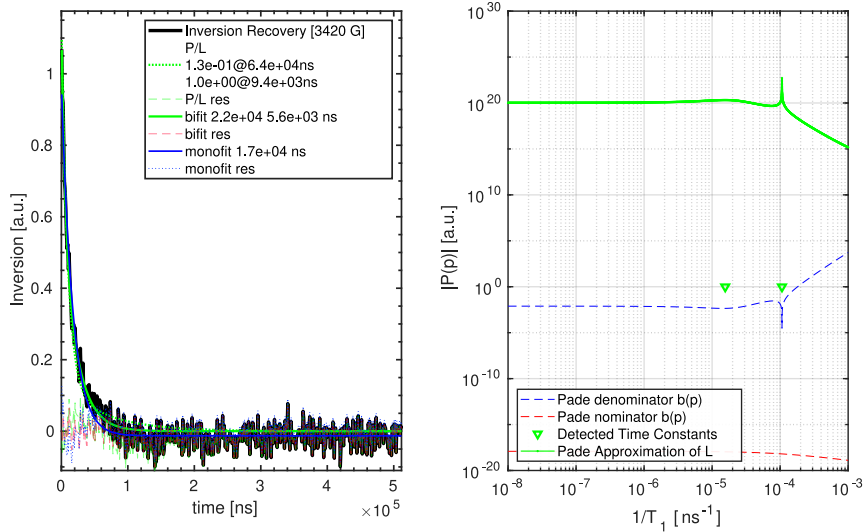


Figure 4.15: Padé-Laplace deconvolution and biexponential fit of the inversion recovery in a pDiTBuS film at 85% ESOC at the $m_I = 0$ spectral position. Temperature 5K. Data is inverted and scaled before fitting.

437 **4.4.2 Detection of Domains with Poor Conductivity**438 **4.4.3 Towards Imaging of Spin Concentration in Battery Electrodes**

439 One can obtain a spatially resolved image of the spin concentrations inside a battery electrode by encoding
 440 the position with a gradient of the magnetic field. With the procedure described in Section 4.4.2 and
 441 using a pair of electromagnetic coils to superimpose a gradient of B_0 one can not only measure the spin
 442 concentrations that are present in the electrode, but also to locate the electrochemically inactive domains
 443 and to visualize the conductive paths throughout the electrode.

444 **4.4.4 Unusual Peak Ratios in a Highly Charged Cathode Film**

445 **Chapter 5**

446 **Longitudinally Detected Electron
Paramagnetic Resonance in Systems
with Short Relaxation Times**

447 448 LOD lets us look behind the protection pulse.

450 **Chapter 6**

451 **Electrically Detected Magnetic
452 Resonance on a Cathode of an Organic
453 Radical Battery**

454 With EDMR we observe the hopping charge as it travels to the charge bearing group through the elec-
455 trode.

456 **6.0.1 Spin Blockade and Spin-Dependent Recombination**

457 **6.0.2 Instrumentation**

458 **6.0.3 Device Fabrication**

459 **1N4007 Si diode**

460 A commercial 1N4007 p-n Si diode was modified to use as a standard for the EDMR experiments. The
461 plastic housing of the diode was opened and the copper leads were etched out to reduce the metal content
462 of the sample that strongly suppresses the B_1 field needed for reaching the resonance condition, and, addition-
463 ally, leads to the heating of the sample which affects the current through the diode. The diode with the
464 opened housing was placed into a droplet of concentrated nitric acid (65% HNO_3) and the etching process
465 was observed in a microscope. When the copper leads have reduced in size so that only a thin layer of
466 copper was covering the Si crystal, the etching reaction was stopped with ethanol. Two $\varnothing 0.1$ mm Ag wires
467 were used to connect the diode to the detection circuit through the screened coaxial cables. The device was
468 placed in a $\varnothing 4.9$ mm OD quartz EPR sample tube.

469

470 **DPP-DTT Organic Ambipolar Field Effect Transistor**

471 An organic field-effect transistor was fabricated by Z. Wang in the Cavendish Laboratory of the University
472 of Cambridge in a glovebox filled with Ar. A 3.5 mm wide, 1 mm thick quartz substrate was carrying two
473 on-substrate meander-shaped Au electrodes as the drain and the source electrodes. A thin film of DPP-DTT
474 was spin-coated on the on-substrate electrodes. A layer of ???? was spin-coated as the gate isolator on top
475 of the DPP-DTT film. The Au gate electrode was evaporated onto the isolator layer through a shadow
476 mask. The metal electrodes were extended with a wire bonder, and soldered to thick Cu wires. The device
477 was encapsulated in a $\varnothing 4.9$ mm OD quartz EPR sample tube.

478 **pDiTBuS Organic Radical Battery**

479 **6.0.4 EDMR signal in a 1N4007 Si Diode**

480 **6.0.5 EDMR signal in an Organic Field Effect Transistor**

481 **6.0.6 EDMR signal in a TEMPO-Salen Electrochemical Cell**

482 **6.0.7 Distribution of Current Density in On-Substrate Meander-Shaped Electrodes**

483 Meander-shaped electrodes shown in Figure 6.1 are used to study properties of thin conductive films. The
 484 distribution of electric potential and the current within a film of poor conductivity and a finite thickness be
 485 not obvious.

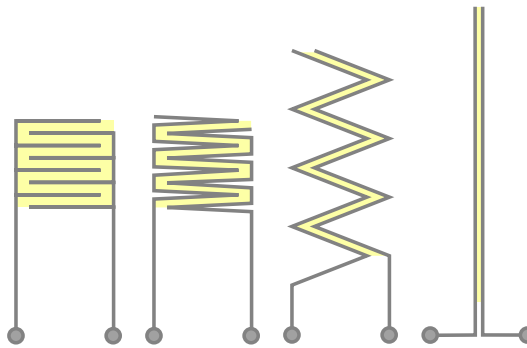


Figure 6.1: Transformation of the meander-shaped electrode grid into two linear electrodes

486 A numerical solution was found to the distribution of the current density \vec{j} within a film of a finite
 487 thickness, connected by two metal electrodes. Two cases were considered, a thick film and a thin film.

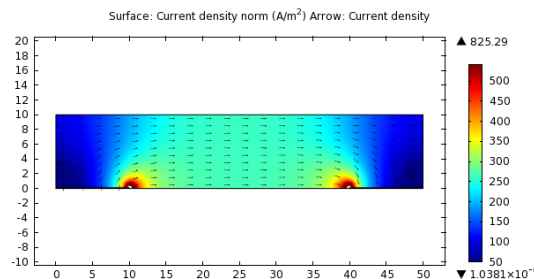


Figure 6.2: Distribution of electric current in a thick polymer film. The current is uniform in the middle of the film. **Let us see, whether we can apply the simple, bulk formula to this structure.**

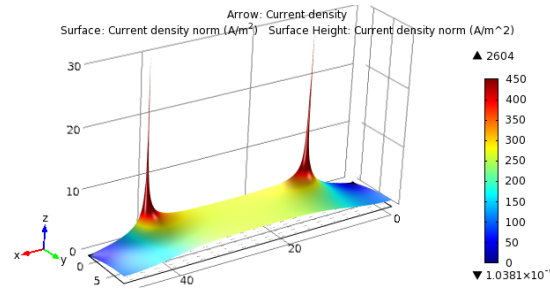


Figure 6.3: Thick film. The current is uniform in the middle of the film. It is better seen on this 3d plot. Let us see, whether we can apply the simple, bulk formula to this structure. I think we do not gain a lot of error by saying that the current is uniform within the whole film.

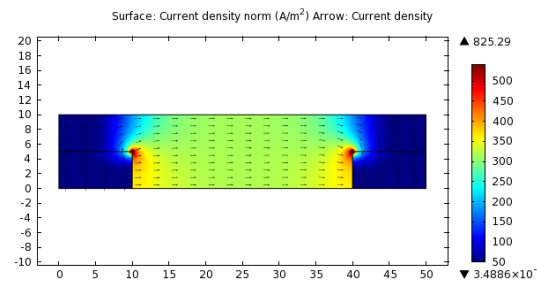


Figure 6.4: Distribution of electric current in an intermediate polymer film

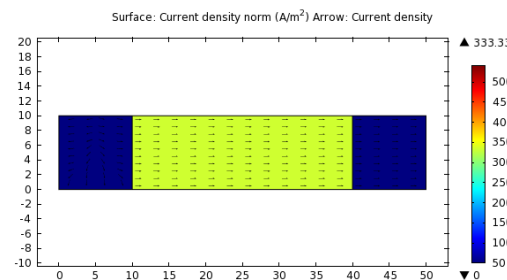


Figure 6.5: Distribution of electric current in a thin polymer film

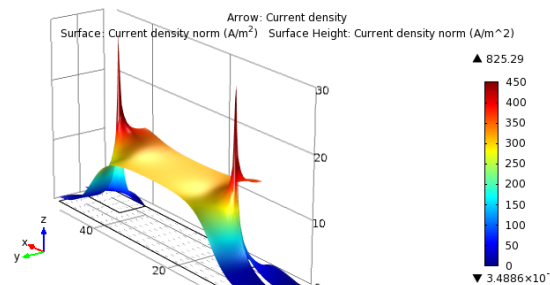


Figure 6.6: Very high values of the computed distribution of the current density in a film of intermediate thickness due to the sharp edges of the contacts.

488

Chapter 7

489

490

The Deep-Trap Model of a TEMPO-Salen Electrode Film

491

A TEMPO-Salen redox conductive film can be seen as a p-type molecular semiconductor enriched with hole traps. The conductive Salen backbone is carrying positive polarons and bipolarons that delocalize within the polymer fragments and effectively hop between them. When a polaron, traveling through the Salen backbone, approaches a charge-bearing TEMPO[•] fragment, it rather hops to it, recombining with the unpaired electron of the radical. The TEMPO[•] oxidizes and becomes TEMPO⁺ which now bears a positive charge. Therefore, TEMPO[•] is a trap for the positive charge carrier (hole) that is injected into the poly-Salen network.

492

The charging of a TEMPO-Salen cathode film can be seen as a consequent filling of traps in a hole-transporting semiconductor. The relative orientations of the spins of the recombining particles defines the probability of the recombination process. At low SoC, the hole, traveling through the polymer, has many TEMPO[•] candidates to recombine with. Some of the TEMPO[•] radicals are in the $|\uparrow\rangle$ state, some are in the $|\downarrow\rangle$ state, - so the recombination process does not depend on the spin state of the hole, as it can recombine to the radical in the “appropriate” spin state. At higher SoC, the more TEMPO[•] become occupied with holes and become TEMPO⁺, the longer distance the hole needs to overcome to meet the TEMPO[•] that has the “appropriate” spin state. In this case, the recombination process must become spin dependent and an EDMR signal appears.

493

no edmr data to prove that, yet. The short distance between the TEMPO[•] in the TEMPO-Salen film leads to the strong exchange interaction between the neighboring TEMPO[•]. That leads to the anti-parallel alignment of their spins and makes them EPR silent and causes a drastic difference between the Coulomb counting and the ESOC data. The formation of bipolarons in the Salen backbone and the close packing of TEMPO[•] may lead to the two-hole-two-electron recombination that can explain the high charging rates of TEMPO-Salen films.

513

Chapter 8

514

Conclusions and Outlook

515

What hasn't worked so far is the EDMR. It would be super cool to see the signal, but my devices don't live that long. LOD also did not work up to now. Adjusting the pulse train rate to the eigenfrequency of the ENDOR coils turned out to be an irresistible obstacle.

516

517

Bibliography

- 518 [1] Robert Bittl and Stefan Weber. Transient radical pairs studied by time-resolved epr. *Biochimica et*
519 *Biophysica Acta - Bioenergetics*, 1707:117–126, 2005.
- 521 [2] Nerea Casado and David Mecerreyes. Chapter 1: Introduction to redox polymers: Classification,
522 characterization methods and main applications, 2021.
- 523 [3] Florian Degen and Marius Schütte. Life cycle assessment of the energy consumption and ghg
524 emissions of state-of-the-art automotive battery cell production. *Journal of Cleaner Production*,
525 330:129798, 2022.
- 526 [4] Boucar Diouf and Christophe Avis. The potential of li-ion batteries in ecowas solar home systems.
527 *Journal of Energy Storage*, 22:295–301, 2019.
- 528 [5] Evgenia Dmitrieva, Marco Rosenkranz, Julia S. Danilova, Evgenia A. Smirnova, Mikhail P. Karu-
529 shhev, Irina A. Chepurnaya, and Aleksander M. Timonov. Radical formation in polymeric nickel
530 complexes with n2o2 schiff base ligands: An in situ esr and uv-vis-nir spectroelectrochemical study.
531 *Electrochimica Acta*, 283:1742–1752, 2018.
- 532 [6] M. Fehr, J. Behrends, S. Haas, B. Rech, K. Lips, and A. Schnegg. Electrical detection of electron-spin-
533 echo envelope modulations in thin-film silicon solar cells. *Physical Review B - Condensed Matter and*
534 *Materials Physics*, 84:1–5, 11 2011.
- 535 [7] C Fribe and U S Schubert. High-power-density organic radical batteries. *Topics in Current Chem-*
536 *istry*, 375:1–35, 2017.
- 537 [8] Yangyang Fu, Song Lu, Kaiyuan Li, Changchen Liu, Xudong Cheng, and Heping Zhang. An exper-
538 imental study on burning behaviors of 18650 lithium ion batteries using a cone calorimeter. *Journal*
539 *of Power Sources*, 273:216–222, 1 2015.
- 540 [9] Walther Gerlach and Otto Stern. Der experimentelle nachweis der richtungsquantelung im magnet-
541 feld. *Zeitschrift für Physik*, 9:348–352, 1922.
- 542 [10] Nicolas Goujon, Nerea Casado, Nagaraj Patil, Rebeca Marcilla, and David Mecerreyes. Organic
543 batteries based on just redox polymers: Abstract. *Progress in Polymer Science*, 122:101449, 2021.
- 544 [11] Cristina Grosu, Chiara Panosetti, Steffen Merz, Peter Jakes, Stefan Seidlmaier, Sebastian Matera,
545 Rüdiger a Eichel, Josef Granwehr, and Christoph Scheurer. Revisiting the storage capacity limit of
546 graphite battery anodes : Spontaneous lithium overintercalation at ambient pressure. *PRX Energy*,
547 2:1–14, 2023.
- 548 [12] Ting Guan, Shun Sun, Fengbin Yu, Yunzhi Gao, Peng Fan, Pengjian Zuo, Chunyu Du, and Geping
549 Yin. The degradation of licoo2/graphite batteries at different rates. *Electrochimica Acta*, 279:204–
550 212, 2018.
- 551 [13] Edward H. Hellen. Padé-laplace analysis of signal averaged voltage decays obtained from a simple
552 circuit. *American Journal of Physics*, 73:871–875, 9 2005.

- 553 [14] Takuma Hirasawa, Mika Yoshida, and Shin'ya Obara. Battery control for leveling the amount of
554 electricity purchase in smart-energy houses. *International Journal of Energy Research*, 45:807–823,
555 2021.
- 556 [15] Q Huang, E D Walter, L Cosimescu, D Choi, and J P Lemmon. In situ electrochemical-electron
557 spin resonance investigations of multi-electron redox reaction for organic radical cathodes. *Journal
558 of Power Sources*, 306:812–816, 2016.
- 559 [16] T Janoschka, M D Hager, and U S Schubert. Powering up the future: Radical polymers for battery
560 applications. *Adv. Mater.*, 24:6397–6409, 2012.
- 561 [17] Tobias Janoschka, Christian Friebe, Martin D. Hager, Norbert Martin, and Ulrich S. Schubert. An
562 approach toward replacing vanadium: A single organic molecule for the anode and cathode of an
563 aqueous redox-flow battery. *ChemistryOpen*, 6:216–220, 2017.
- 564 [18] Tobias Janoschka, Christian Friebe, Martin D. Hager, Norbert Martin, and Ulrich S. Schubert. An
565 approach toward replacing vanadium: A single organic molecule for the anode and cathode of an
566 aqueous redox-flow battery. *ChemistryOpen*, 6:216–220, 2017.
- 567 [19] G Jeschke. Deer distance measurements on proteins. *Annual Review of Physical Chemistry*, Vol 63,
568 63:419–446, 2012.
- 569 [20] Josef Kadlec, Radoslav Cipin, Dalibor Cervinka, Pavel Vorel, and Bohumil Klima. Li-ion accumula-
570 tors for propulsion system of electric airplane vut 051 ray. *Journal of Solid State Electrochemistry*,
571 18:2307–2313, 2014.
- 572 [21] Jihyeon Kim, Youngsu Kim, Jaekyun Yoo, Giyun Kwon, Youngmin Ko, and Kisuk Kang. Organic
573 batteries for a greener rechargeable world. *Nature Reviews Materials*, 8:54–70, 2023.
- 574 [22] Ilia Kulikov, Naitik A. Panjwani, Anatoliy A. Vereshchagin, Domenik Spallek, Daniil A. Lukianov,
575 Elena V. Alekseeva, Oleg V. Levin, and Jan Behrends. Spins at work: probing charging and dis-
576 charging of organic radical batteries by electron paramagnetic resonance spectroscopy. *Energy and
577 Environmental Science*, 15:3275–3290, 2022.
- 578 [23] Ilya Kuprov. *Spin: From Basic Symmetries to Quantum Optimal Control*. Springer International
579 Publishing, 1 2023.
- 580 [24] T. Kushida and J. C. Murphy. Volume dependence of the knight shift in lithium. *Physical Review B*,
581 21:4247–4250, 1980.
- 582 [25] Fredrik Larsson, Petra Andersson, Per Blomqvist, and Bengt Erik Mellander. Toxic fluoride gas
583 emissions from lithium-ion battery fires. *Scientific Reports*, 7:1–13, 12 2017.
- 584 [26] Yong Hee Lee, Joo Seong Kim, Jonghyeon Noh, Inhwa Lee, Hyeong Jun Kim, Sunghun Choi, Jeong-
585 min Seo, Seokwoo Jeon, Taek Soo Kim, Jung Yong Lee, and Jang Wook Choi. Wearable textile
586 battery rechargeable by solar energy. *Nano Letters*, 13:5753–5761, 2013.
- 587 [27] Chao Li, Ming Shen, and Bingwen Hu. Solid-state nmr and epr methods for metal ion battery re-
588 search. *Wuli Huaxue Xuebao/Acta Physico - Chimica Sinica*, 36:1–16, 2019.
- 589 [28] Yong Lu and Jun Chen. Prospects of organic electrode materials for practical lithium batteries. *Nature
590 Reviews Chemistry*, 4:127–142, 2020.
- 591 [29] Tianyi Ma, Siyuan Wu, Fang Wang, Joseph Lacap, Chunjing Lin, Shiqiang Liu, Mohan Wei, Weijian
592 Hao, Yunshi Wang, and Jae Wan Park. Degradation mechanism study and safety hazard analysis
593 of overdischarge on commercialized lithium-ion batteries. *ACS Applied Materials and Interfaces*,
594 12:56086–56094, 2020.

- 595 [30] Praveen Kumar Reddy Maddikunta, Gautam Srivastava, Thippa Reddy Gadekallu, Natarajan Deepa,
596 and Prabadevi Boopathy. Predictive model for battery life in iot networks. *IET Intelligent Transport
597 Systems*, 14:1388–1395, 2020.
- 598 [31] Christoph Meier, Jan Behrends, Christian Teutloff, Oleksandr Astakhov, Alexander Schnegg, Klaus
599 Lips, and Robert Bittl. Multi-frequency edmr applied to microcrystalline thin-film silicon solar cells.
600 *Journal of Magnetic Resonance*, 234:1–9, 2013.
- 601 [32] Alice J. Merryweather, Quentin Jacquet, Steffen P. Emge, Christoph Schnedermann, Akshay Rao,
602 and Clare P. Grey. Operando monitoring of single-particle kinetic state-of-charge heterogeneities and
603 cracking in high-rate li-ion anodes. *Nature Materials*, 21:1306–1313, 2022.
- 604 [33] S Muench, A Wild, C Friebe, B Haupler, T Janoschka, and U S Schubert. Polymer-based organic
605 batteries. *Chemical Reviews*, 116:9438–9484, 2016.
- 606 [34] K Nakahara, S Iwasa, M Satoh, Y Morioka, J Iriyama, M Suguro, and E Hasegawa. Rechargeable
607 batteries with organic radical cathodes. *Chem. Phys. Lett.*, 359:351–354, 2002.
- 608 [35] Arvid Niemöller, Peter Jakes, Rüdiger A. Eichel, and Josef Granwehr. In operando epr investigation
609 of redox mechanisms in licoo2. *Chemical Physics Letters*, 716:231–236, 2019.
- 610 [36] Arvid Niemöller, Peter Jakes, Svitlana Eurich, Anja Paulus, Hans Kungl, Rüdiger A. Eichel, and
611 Josef Granwehr. Monitoring local redox processes in lini0.5mn1.5o4 battery cathode material by in
612 operando epr spectroscopy. *Journal of Chemical Physics*, 148:1–10, 2018.
- 613 [37] Hiroyuki Nishide, Kenichiro Koshika, and Kenichi Oyaizu. Environmentally benign batteries based
614 on organic radical polymers. volume 81, pages 1961–1970, 2009.
- 615 [38] Naoki Nitta, Feixiang Wu, Jung Tae Lee, and Gleb Yushin. Li-ion battery materials: Present and
616 future. *Materials Today*, 18:252–264, 2015.
- 617 [39] Jens F. Peters, Manuel Baumann, Benedikt Zimmermann, Jessica Braun, and Marcel Weil. The
618 environmental impact of li-ion batteries and the role of key parameters – a review. *Renewable and
619 Sustainable Energy Reviews*, 67:491–506, 2017.
- 620 [40] M. H. Poincaré. Sur la dynamique de l'électron. *Rend. Circ. Matem. Palermo*, pages 129–175, 12
621 1906.
- 622 [41] Anna Pražanová, Vaclav Knap, and Daniel Ioan Stroe. Literature review, recycling of lithium-ion
623 batteries from electric vehicles, part i: Recycling technology. *Energies*, 15:1–29, 2022.
- 624 [42] Kevin J. Rhodes, Roberta Meisner, Melanie Kirkham, Nancy Dudney, and Claus Daniel. In situ xrd of
625 thin film tin electrodes for lithium ion batteries. *Journal of The Electrochemical Society*, 159:A294–
626 A299, 2012.
- 627 [43] K. M. Salikhov, S. A. Dzuba, and A. M. Raitsimring. The theory of electron spin-echo signal decay
628 resulting from dipole-dipole interactions between paramagnetic centers in solids. *Journal of Magnetic
629 Resonance*, 42:255–276, 1981.
- 630 [44] K M Salikhov and N E Zavoiskaya. Zavoisky and the discovery of epr, 2015.
- 631 [45] A Schweiger and G Jeschke. *Principles of Pulse Electron Paramagnetic Resonance*. Oxford University
632 Press, 2001.
- 633 [46] A Schweiger and G Jeschke. *Principles of Pulse Electron Paramagnetic Resonance*. Oxford University
634 Press, 2001.
- 635 [47] Yongchao Shi and Mingxue Tang. Nmr/epr investigation of rechargeable batteries. *Wuli Huaxue
636 Xuebao/Acta Physico - Chimica Sinica*, 36:1–13, 2019.

- 637 [48] Hiroyuki Takeo Nishide and Suga. Organic radical battery. *Journal of the Society of Mechanical*
638 *Engineers*, 110:194–195, 2007.
- 639 [49] Yu. V. Toropov, S. A. Dzuba, Yu. D. Tsvetkov, V Monaco, F Formaggio, M Crisma, C Toniolo, and
640 J. Raap. Molecular dynamics and spatial distribution of toac spin-labelled peptaibols studied in glassy
641 liquid by echo-detected epr spectroscopy. *Applied Magnetic Resonance*, 15:237–246, 1998.
- 642 [50] Anatolii. A. Vereshchagin, Daniil A. Lukyanov, Ilia R. Kulikov, Naitik A. Panjwani, Elena A. Alek-
643 seeva, Jan Behrends, and Oleg V. Levin. The fast and the capacious: A [ni(salen)]-tempo redox-
644 conducting polymer for organic batteries. *Batteries & Supercaps*, 4:336–346, 2020.
- 645 [51] Anatoliy A. Vereshchagin, Arseniy Y. Kalnin, Alexey I. Volkov, Daniil A. Lukyanov, and Oleg V.
646 Levin. Key features of tempo-containing polymers for energy storage and catalytic systems. *Energies*,
647 15:1–50, 2022.
- 648 [52] Yuan Xie, Kai Zhang, Yusuke Yamauchi, Kenichi Oyaizu, and Zhongfan Jia. Nitroxide radical poly-
649 mers for emerging plastic energy storage and organic electronics: Fundamentals, materials, and ap-
650 plications. *Materials Horizons*, 8:803–829, 2021.
- 651 [53] Chengjian Xu, Qiang Dai, Linda Gaines, Mingming Hu, Arnold Tukker, and Bernhard Steubing.
652 Future material demand for automotive lithium-based batteries. *Communications Materials*, 1:1–10,
653 2020.
- 654 [54] Hyun Deog Yoo, Elena Markevich, Gregory Salitra, Daniel Sharon, and Doron Aurbach. On the
655 challenge of developing advanced technologies for electrochemical energy storage and conversion.
656 *Materials Today*, 17:110–121, 2014.
- 657 [55] E K Zavoisky. Paramagnetic relaxation of liquid solutions for perpendicular fields. *Zhur. Eksperiment.*
658 *i Theoret. Fiz.*, 15:344–350, 1945.
- 659 [56] Clara Zens, Christian Friebel, Ulrich S. Schubert, Martin Richter, and Stephan Kupfer. Tailored charge
660 transfer kinetics in precursors for organic radical batteries – a joint synthetic-theoretical approach.
661 *ChemSusChem*, e202201679:1–14, 2022.
- 662 [57] Guangxu Zhang, Xuezhe Wei, Siqi Chen, Guangshuai Han, Jiangong Zhu, and Haifeng Dai. Investiga-
663 tion the degradation mechanisms of lithium-ion batteries under low-temperature high-rate cycling.
664 *ACS Applied Energy Materials*, 5:6462–6471, 2022.
- 665 [58] Qingsong Zhang, Tiantian Liu, and Qiong Wang. Experimental study on the influence of different
666 heating methods on thermal runaway of lithium-ion battery. *Journal of Energy Storage*, 42:1–9, 10
667 2021.